





Non-Standard Interactions and Light Z' Bosons from $\text{CE}\nu\text{NS}$ Data at CONUS+: A Statistical Analysis

Ch. M. Benavides ^{1, a}, C. S. Muñoz ^{1, b}, B.C. Cañas ^{2, c} and E. Rojas ^{1, d}

¹*Departamento de Física, Universidad de Nariño, Pasto, Colombia*

²*Departamento de Física, Universidad de Pamplona, Pamplona, Colombia*

(Dated: June 22nd, 2026)

Motivated by the recent results reported by the CONUS+ collaboration, in which coherent elastic neutrino-nucleus scattering ($\text{CE}\nu\text{NS}$) with reactor antineutrinos was observed for the first time, we perform a statistical analysis to constrain possible low-energy scenarios of physics beyond the Standard Model (BSM). The models considered include effective non-standard vector interactions of neutrinos (NSI) and generalized neutrino interactions (NGI) by light vector bosons within the E_6 and $U(1)_{L_e-L_\mu}$ frameworks.

I. INTRODUCTION

$\text{CE}\nu\text{NS}$ is a standard model (SM) process in which a neutrino interacts coherently and elastically with an atomic nucleus. This process was theoretically predicted by Daniel Z. Freedman in 1974 [1] and was discovered in 2017 by the COHERENT collaboration using a CsI[Na] detector [2]. Subsequent new observations of $\text{CE}\nu\text{NS}$ have been reported by COHERENT using a liquid argon detector in 2021 [3] and a germanium detector in 2025 [4]. In all these experiments, a neutrino source from the Spallation Neutron Source (SNS) is used. In parallel, the PandaX and XENONnT dark-matter experiments detected solar $\text{CE}\nu\text{NS}$ in liquid xenon in 2024 [5, 6]. Recently, the CONUS+ collaboration reported the first direct observation of $\text{CE}\nu\text{NS}$ with a reactor antineutrino source, with a statistical significance of (3.7σ) [7].

Based on the results reported by the CONUS+ collaboration, several phenomenological studies have been carried out to evaluate the sensitivity of $\text{CE}\nu\text{NS}$ not only as a precision electroweak test, but also to various low-momentum-transfer new-physics scenarios, such as electromagnetic properties of neutrinos, sterile neutrinos, up-scattering production of a sterile fermion, NSI, among others [8–12]. In this work, we have focused on scenarios for light vector bosons Z' with well-defined charge assignments, considering E_6 benchmark models and leptophilic models, and show that our results provide complementary low-energy constraints to collider searches and electroweak precision measurements.

Unlike many generic Z' scenarios that are severely constrained by LHC searches, the anomaly-free leptophilic symmetries [13] $L_{\ell_i} - L_{\ell_j}$ evade most collider limits because their couplings to quarks are absent or highly suppressed. Existing bounds on these models have therefore been mainly obtained from low-energy neutrino-scattering observables, including solar-neutrino elastic scattering on electrons, electron-recoil data in liquid-xenon direct-detection experiments, and neutrino-trident production [14–18]. In the light-mediator regime, typically around $m_{Z'} \lesssim 10^{-3}$ MeV, these probes can reach upper limits of order $g_{Z'} \sim 10^{-7}$, as reported in analyses based on Borexino, PandaX-4T, XENONnT, and LUX-ZEPLIN data [14–17]. In this context, $\text{CE}\nu\text{NS}$ provides a complementary

^a chmbenavides@gmail.com

^b cristiansantiagocsm123@gmail.com

^c blanca.canas@unipamplona.edu.co

^d erojas@udenar.edu.co

nuclear-recoil channel: although leptophilic Z' bosons do not couple to quarks at tree level, loop-induced A – Z' kinetic mixing generates an effective interaction with the nuclear electromagnetic current, allowing reactor $\text{CE}\nu\mathcal{N}\text{S}$ data to constrain the same gauge coupling through a different observable [19, 20].

In this work, we employ the first CONUS+ dataset to derive constraints on: (i) NSI between neutrinos and first-generation quarks; (ii) a generic light vector Z' mediator; (iii) E_6 -motivated Z' models in the Sanson–Flamsteed (SF) parametrization; and (iv) the leptophilic $U(1)_{L_e-L_\mu}$ model including kinetic mixing. The paper is structured as follows: [section II](#) introduces the theoretical formalism, [section III](#) summarizes the CONUS+ experimental setup and describes the statistical analysis, [section IV](#) presents our results, and [section V](#) summarizes our conclusions.

II. THEORETICAL FORMALISM

In this section, we present the main theoretical aspects relevant to this work. We begin with $\text{CE}\nu\mathcal{N}\text{S}$, and then we extend the formalism to include NSI as a model-independent approach. Next, we focus on neutrino generalized interactions via a light Z' , first in the context of a generic vector mediator, then in E_6 Z' models, and finally in leptophilic $U(1)_{L_e-L_\mu}$ models. In each case, we present the differential cross section that we will consider in the next section.

A. $\text{CE}\nu\mathcal{N}\text{S}$ cross section

$\text{CE}\nu\mathcal{N}\text{S}$ is a SM neutral-current process

$$\nu_\ell + \frac{A}{Z}\mathcal{N} \rightarrow \nu_\ell + \frac{A}{Z}\mathcal{N}, \quad \ell = e, \mu, \tau. \quad (1)$$

At the fundamental level, neutrinos interact with quarks through the exchange of a Z^0 boson; however, in the coherent regime, the momentum transfer is small enough that the internal structure of the nucleus is not resolved. Here, the momentum transferred in the interaction is smaller than the inverse of the size of the nucleus; as a result, the scattering amplitudes of the nucleons add up coherently [1]. The dominant contribution is the vector nuclear current, while axial contributions are not coherently enhanced and are neglected in the present analysis.

The SM prediction for the differential cross section of $\text{CE}\nu\mathcal{N}\text{S}$ as a function of the nuclear recoil energy $T_{\mathcal{N}}$ reads¹

$$\left. \frac{d\sigma_{\nu-\mathcal{N}}}{dT_{\mathcal{N}}} \right|_{\text{SM}} = \frac{G_F^2 m_{\mathcal{N}}}{\pi} (Q_V^{\text{SM}})^2 F_W^2(|\mathbf{q}|^2) \left[1 - \frac{m_{\mathcal{N}} T_{\mathcal{N}}}{2E_\nu^2} - \frac{T_{\mathcal{N}}}{E_\nu} \right], \quad (2)$$

where G_F is the Fermi constant, $m_{\mathcal{N}}$ is the target nuclear mass, E_ν is the incoming neutrino energy and $|\mathbf{q}| \simeq \sqrt{2MT_{\mathcal{N}}}$ is the magnitude of the momentum transfer. The tree-level weak nuclear charge is given by

$$Q_V^{\text{SM}} = g_V^p Z + g_V^n N, \quad (3)$$

with Z and N being the numbers of protons and neutrons in the nucleus, respectively, g_V^p and g_V^n represent the neutrino-nucleon couplings, which correspond to

$$g_V^p = \frac{1 - 4 \sin^2 \theta_W}{2}, \quad g_V^n = -\frac{1}{2}, \quad (4)$$

¹ In this work we employ natural units so that $\hbar = c = 1$.

where θ_W is the weak mixing angle, with $\sin^2 \theta_W = 0.23857(5)$, for the low-energy regime relevant to $\text{CE}\nu\mathcal{N}\text{S}$ [21]. The weak nuclear form factor $F_W(|\mathbf{q}|^2)$ encodes the spatial distribution of the weak charge inside the nucleus and describes the progressive loss of coherence as the momentum transfer $|\mathbf{q}|$ increases. In the low-energy regime relevant for reactor antineutrinos ($E_\nu \lesssim 10$ MeV), the typical momentum transfer satisfies: $|\mathbf{q}|R_A \ll 1$, which implies $F_W(|\mathbf{q}|^2) \simeq 1$.

B. Neutrino Non-Standard Interactions

NSI provides a model-independent parametrization of new-physics effects at low energies, encoded in effective four-fermion operators [22–24]. Since $\text{CE}\nu\mathcal{N}\text{S}$ is a neutral-current process [25–27], only neutral-current NSI are considered. The corresponding effective Lagrangian is given by [28]

$$\mathcal{L}_{\text{NC}}^{\text{NSI}} = -2\sqrt{2}G_F \sum_{\ell, \ell'} \varepsilon_{\ell\ell'}^{fC} (\bar{\nu}_\ell \gamma^\mu P_L \nu_{\ell'}) (\bar{\psi} \gamma_\mu P_C \psi), \quad (5)$$

where $\ell, \ell' = e, \mu, \tau$ denotes flavor indices, $C = L, R$ indicates chirality, and ψ represents SM fermions. The parameters $\varepsilon_{\ell\ell'}^{fC}$ quantify the strength of the NSI relative to the Fermi interaction. These include both non-universal ($\ell = \ell'$) and flavor-changing ($\ell \neq \ell'$) contributions. Since axial contributions are suppressed in $\text{CE}\nu\mathcal{N}\text{S}$ [8, 29], only vector interactions are retained, defined as

$$\varepsilon_{\ell\ell'}^{fV} = \varepsilon_{\ell\ell'}^{fL} + \varepsilon_{\ell\ell'}^{fR}. \quad (6)$$

In this framework, the $\text{CE}\nu\mathcal{N}\text{S}$ differential cross section (2) is modified through a redefinition of the weak charge at the amplitude level. The squared effective charge, including NSI contributions, is given by [8, 30]

$$\begin{aligned} (Q_V^{\text{NSI}})^2 &= \left[Z \left(g_V^p + 2\varepsilon_{\ell\ell}^{uV} + \varepsilon_{\ell\ell}^{dV} \right) + N \left(g_V^n + \varepsilon_{\ell\ell}^{uV} + 2\varepsilon_{\ell\ell}^{dV} \right) \right]^2 \\ &+ \sum_{\ell \neq \ell'} \left[Z \left(2\varepsilon_{\ell\ell'}^{uV} + \varepsilon_{\ell\ell'}^{dV} \right) + N \left(\varepsilon_{\ell\ell'}^{uV} + 2\varepsilon_{\ell\ell'}^{dV} \right) \right]^2. \end{aligned} \quad (7)$$

This expression explicitly shows that diagonal NSI ($\ell = \ell'$) interfere coherently with the SM contribution, while off-diagonal terms ($\ell \neq \ell'$) contribute incoherently at the level of the squared amplitude. In the analysis of CONUS+ reactor antineutrino data, the incoming neutrino flavor is $\ell = e$. Consequently, the relevant NSI parameters are $\varepsilon_{e\ell'}^{uV}$ and $\varepsilon_{e\ell'}^{dV}$, where $\ell' = e, \mu, \tau$.

C. Neutrino Generalized Interactions via a Light Z'

1. Generic vector mediator

A new neutral vector boson Z' with mass $M_{Z'}$ is considered. Its interaction Lagrangian with SM fermions is written as [31]

$$\mathcal{L}_{Z'}^{\text{int}} = -\frac{g_{Z'}}{2} \sum_{\psi} \bar{\psi} \gamma^\mu [g_V^{Z'}(\psi) - g_A^{Z'}(\psi) \gamma^5] \psi Z'_\mu, \quad (8)$$

where $g_{Z'}$ is the coupling constant of the new $U(1)'$ gauge group. The vector and axial-vector coefficients are expressed in terms of the left- and right-handed chiral charges $Q_{L,R}^{Z'}(\psi)$ [32, 33].

$$g_V^{Z'}(\psi) = Q_L^{Z'}(\psi) + Q_R^{Z'}(\psi), \quad g_A^{Z'}(\psi) = Q_L^{Z'}(\psi) - Q_R^{Z'}(\psi). \quad (9)$$

The coherent nuclear matrix element of the Z' vector current can be written in terms of the effective coherent nuclear vector charge[34].

$$Q_{\mathcal{N},V}^{Z'} = Z[2g_V^{Z'}(u) + g_V^{Z'}(d)] + N[g_V^{Z'}(u) + 2g_V^{Z'}(d)], \quad (10)$$

where Z and N are the proton and neutron numbers of the target nucleus. The exchange of Z' then modifies the $\text{CE}\nu\mathcal{N}\text{S}$ cross section (2) as a rescaling of the SM prediction,

$$\frac{d\sigma}{dT_{\mathcal{N}}} = \mathcal{G}_{Z'}^2 \left. \frac{d\sigma}{dT_{\mathcal{N}}} \right|_{\text{SM}}, \quad (11)$$

with the scaling factor [34]

$$\mathcal{G}_{Z'}^2 = \left| 1 + \frac{1}{2\sqrt{2}G_F} \frac{Q_{\mathcal{N},V}^{Z'}}{Q_V^{\text{SM}}} \frac{g_{Z'}^2 g_V^{Z'}(\nu)}{2m_{\mathcal{N}}T_{\mathcal{N}} + M_{Z'}^2} \right|^2. \quad (12)$$

2. E_6 -motivated Z' models

Grand-unified extensions based on E_6 predict additional neutral gauge bosons Z' . In the SF parametrization, the corresponding E_6 charge assignments are mapped onto the angular plane $(\alpha, \beta) \in [-\frac{\pi}{2}, \frac{\pi}{2}]$, so that each benchmark model is represented by a specific direction in parameter space. Following the unification-motivated normalization adopted by Langacker, we take

$$g_{Z'} = \sqrt{\frac{5}{3}} g \tan \theta_W \simeq 0.46, \quad (13)$$

in agreement with Eqs. (44) and (49) of Ref. [31]. The fermion charges in the fundamental **27** representation are listed in Table I.

Table I. Fermion charges in the E_6 fundamental representation. [31]

Field	$2\sqrt{10}Q_{E_6}^X$	$2\sqrt{6}Q_{E_6}^\psi$	$\sqrt{5/3}Q_Y^{E_6}$
ν_L	3	1	-1/2
e_L	3	1	-1/2
e_R	1	-1	-1
u_L	-1	1	1/6
u_R	1	-1	2/3
d_L	-1	1	1/6
d_R	-3	-1	-1/3

In the SF basis, the physical Z' is written as a linear combination of three gauge eigenstates [33],

$$Z' = \cos \alpha \cos \beta Z_\chi + \sin \alpha \cos \beta Z_Y + \sin \beta Z_\psi, \quad (14)$$

which induces the chiral charges

$$Q_{L,R}^{Z'}(\psi) = \cos \alpha \cos \beta Q_{E_6}^X(\psi_{L,R}) + \sin \alpha \cos \beta Q_{E_6}^Y(\psi_{L,R}) + \sin \beta Q_{E_6}^\psi(\psi_{L,R}). \quad (15)$$

The corresponding vector couplings used in the $\text{CE}\nu\mathcal{N}\mathcal{S}$ rate are obtained by Eq. (9)

$$g_V^{Z'}(\nu) = \frac{3}{2\sqrt{10}} \cos\alpha \cos\beta - \frac{1}{2}\sqrt{\frac{3}{5}} \sin\alpha \cos\beta + \frac{1}{2\sqrt{6}} \sin\beta, \quad (16)$$

$$g_V^{Z'}(u) = \frac{5}{6}\sqrt{\frac{3}{5}} \sin\alpha \cos\beta, \quad (17)$$

$$g_V^{Z'}(d) = -\frac{2}{\sqrt{10}} \cos\alpha \cos\beta - \frac{1}{6}\sqrt{\frac{3}{5}} \sin\alpha \cos\beta. \quad (18)$$

Special limiting cases of phenomenological interest, including $B-L$, χ , ψ , and related benchmark directions, are obtained for particular values of (α, β) within the SF basis, as summarized in Table II.

Table II. Charges associated with different $U(1)'$ groups in the SF basis. [33]

$U(1)'$	Z'	$\tan\alpha$	$\tan\beta$
$U(1)_A$	$+Z_{\not{d}}$	$-2\sqrt{6}$	$\sqrt{\frac{3}{5}}$
$U(1)_{21\bar{I}}$	$+Z_{\not{e}}$	$4\sqrt{\frac{2}{3}}$	$-\frac{1}{\sqrt{7}}$
$U(1)_{21\bar{A}}$	$+Z_{\not{p}}$	$\frac{2\sqrt{2/3}}{3}$	$\frac{1}{\sqrt{7}}$
$U(1)_{31R}$	$-Z_{B-L}$	$-\sqrt{\frac{2}{3}}$	0
$U(1)_{31I}$	$-Z_{\not{f}}$	$\frac{2\sqrt{2/3}}{3}$	$-\frac{3}{\sqrt{7}}$
$U(1)_{42R}$	$-Z_{\psi}$	0	∞
$U(1)_{\chi RI}$	$+Z_{\chi}$	0	0

3. Leptophilic models and $A-Z'$ kinetic mixing

Leptophilic extensions of the SM are characterized by the assignment of non-zero $U(1)'$ charges exclusively to leptons, while quarks remain neutral at tree level. As a consequence, the new gauge boson Z' does not couple directly to hadronic matter in the fundamental Lagrangian. The anomaly-free charge assignments most commonly used in the literature are summarized in Table III [13, 17].

Table III. Vector charges $Q_{Z'}$ under the leptophilic $U(1)'$ models considered [13, 17]. The notation Q^{f/ν_f} indicates that the charge is identical for the charged lepton f and its associated neutrino ν_f .

Model	$Q_{Z'}^{e/\nu_e}$	$Q_{Z'}^{\mu/\nu_\mu}$	$Q_{Z'}^{\tau/\nu_\tau}$
$L_e - L_\mu$	+1	-1	0
$L_e - L_\tau$	+1	0	-1
$L_\mu - L_\tau$	0	+1	-1

In the present analysis, the $U(1)_{L_e - L_\mu}$ realization is considered, and the interaction Lagrangian is written as [17, 35]

$$\mathcal{L}_{L_e - L_\mu} \supset g_{Z'} Z'_\mu \left(\bar{\mu} \gamma^\mu \mu - \bar{e} \gamma^\mu e + \bar{\nu}_\mu \gamma^\mu P_L \nu_\mu - \bar{\nu}_e \gamma^\mu P_L \nu_e \right). \quad (19)$$

Since quarks carry no $L_e - L_\mu$ charge, the Z' boson does not couple to nucleons at tree level. Nevertheless, an effective interaction with hadronic matter is generated radiatively through kinetic

mixing with the photon. This effect arises at one-loop level via charged-lepton loops, as illustrated in Figure 1, and induces a momentum-dependent mixing parameter $\varepsilon(q^2, g_{Z'})$ [35]

$$\varepsilon(q^2, g_{Z'}) = \frac{8 e g_{Z'}}{(4\pi)^2} \int_0^1 x(1-x) \ln \left(\frac{m_\mu^2 - x(1-x)q^2}{m_e^2 - x(1-x)q^2} \right) dx. \quad (20)$$

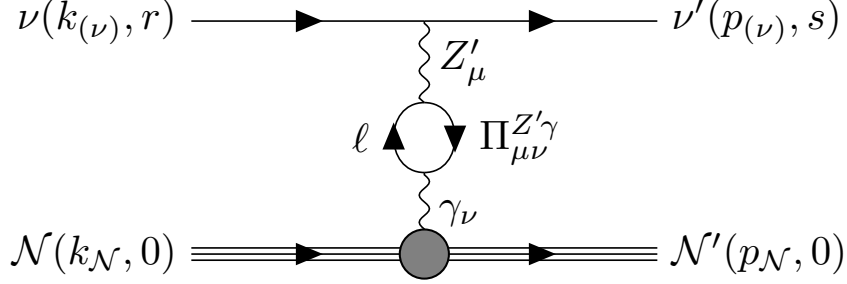


Figure 1. Feynman diagram for $\text{CE}\nu\mathcal{N}\text{S}$ mediated by the mixed A - Z' propagator. The interaction between neutrinos and the nucleus is induced through a leptonic loop, generating kinetic mixing between the photon and the Z' boson.

The origin of this contribution can be understood directly at the level of the effective Lagrangian. The kinetic mixing term between the photon and the new gauge boson is given by

$$\mathcal{L}_{A-Z'}^{\text{int}} = -\frac{\varepsilon}{2} (\partial^\mu Z'^\nu - \partial^\nu Z'^\mu) F_{\mu\nu}, \quad (21)$$

where Z'^μ and A_ν are the extra gauge boson and the photon fields, respectively, and $F_{\mu\nu}$ is the electromagnetic field-strength tensor.

After integrating by parts, discarding total derivatives, and imposing the Lorenz gauge condition $\partial^\mu A_\mu = 0$, this term can be rewritten in momentum space as

$$\mathcal{L}_{A-Z'}^{\text{int}} = \varepsilon Z'^\nu \square A_\nu. \quad (22)$$

which leads to the mixed vertex

$$V_{\mu\nu} = -i\varepsilon q^2 g_{\mu\nu}. \quad (23)$$

Combining this vertex with the free propagators of the photon and the Z' boson, one obtains the effective mixed propagator

$$i\Pi_{\mu\nu} = \left(\frac{-ig_{\mu\alpha}}{q^2 - m_{Z'}^2} \right) (-i\varepsilon q^2 g^{\alpha\beta}) \left(\frac{-ig_{\beta\nu}}{q^2} \right) = \frac{i\varepsilon g_{\mu\nu}}{q^2 - m_{Z'}^2}. \quad (24)$$

This structure makes it explicit that the interaction between neutrinos and the nucleus is mediated by the Z' boson via its mixing with the photon, thereby generating a coupling to the nuclear electromagnetic current.

Using Eq. (24), the $\text{CE}\nu\mathcal{N}\text{S}$ scattering amplitude induced by the Z' photon mixing can be written as

$$\mathcal{M}_{L_e-L_\mu} = \frac{(i)^3}{2} \frac{e g_{Z'} g_V^{Z'}(\nu) \varepsilon}{q^2 - m_{Z'}^2 - i\epsilon} Q_{\mathcal{N}}^A F(q^2) \bar{u}_s(p_\nu) \gamma^\mu (1 - \gamma^5) u_r(k_\nu) (p_{\mathcal{N}} + k_{\mathcal{N}})_\mu, \quad (25)$$

where Q_N^A denotes the nuclear electric charge, equal to the number of protons Z in the target nucleus, and $F(q^2)$ is the nuclear electromagnetic form factor.

It is convenient to express the result in terms of a multiplicative correction to the SM contribution. Using the relation

$$\frac{d\sigma}{dT_N} = \frac{|\mathcal{M}|^2}{32\pi m_N E_\nu^2}, \quad (26)$$

which follows from the standard treatment of $2 \rightarrow 2$ scattering processes based on Fermi's Golden Rule [36, 37]. In this expression, $|\mathcal{M}|^2$ represents the spin-summed and spin-averaged squared invariant matrix element. The differential cross section can be written as

$$\frac{d\sigma}{dT_N} = \mathcal{G}_{L_e-L_\mu}^2 \left. \frac{d\sigma}{dT_N} \right|_{\text{SM}}, \quad \mathcal{G}_{L_e-L_\mu}^2 = \left[1 + \frac{\sqrt{2}}{G_F} \frac{e g_{Z'} \varepsilon}{q^2 - m_{Z'}^2} \frac{Q_N^A}{Q_V^{\text{SM}}} \right]^2. \quad (27)$$

This result explicitly shows how the leptophilic interaction modifies the $\text{CE}\nu\mathcal{N}\text{S}$ cross section via an effective coupling to the nuclear electromagnetic current, with the momentum dependence governed by the propagator structure and the loop-induced mixing parameter.

III. STATISTICAL ANALYSIS

In this section, we present the statistical analysis of CONUS+ data used to constrain the scenarios under study in this work. We closely follow the methodology applied in Ref. [8]. We also present in detail the main experimental characteristics and the required parameters.

A. The CONUS+ Experiment

The CONUS+ experiment has reported the first observation of $\text{CE}\nu\mathcal{N}\text{S}$ with antineutrinos, with a statistical significance of 3.7σ [7]. For detection, CONUS+ used high-purity germanium detectors with kilogram-scale masses and very low keV-range thresholds. These detectors are located 21 m from the Leibstadt nuclear reactor in Switzerland. This discovery enables precision tests of standard-model parameters, such as the weak mixing angle, and the exploration of new physical scenarios beyond the standard model, as considered in this work.

Table IV summarizes the experimental input parameters from CONUS+ used to determine the predicted $\text{CE}\nu\mathcal{N}\text{S}$ event rates discussed in the next section.

B. $\text{CE}\nu\mathcal{N}\text{S}$ event rate

The predicted number of $\text{CE}\nu\mathcal{N}\text{S}$ signal events in the i -th reconstructed ionization-energy bin is given by

$$R_i^{\text{th}} = \int_{E_i^{\text{low}}}^{E_i^{\text{high}}} \frac{dR}{dE_{\text{ee}}^{\text{reco}}} dE_{\text{ee}}^{\text{reco}}, \quad (28)$$

where the bin edges $E_i^{\text{low}}, E_i^{\text{high}}$ are given in electron-equivalent energy (eV_{ee}). The reconstructed-energy bins span the interval 160–350 eV_{ee} in steps of 10 eV_{ee} . The observable quantity is the reconstructed electron-equivalent energy $E_{\text{ee}}^{\text{reco}}$, which is related to the underlying nuclear recoil energy T_N through detector effects. Since the $\text{CE}\nu\mathcal{N}\text{S}$ cross section is fundamentally expressed in

Table IV. Experimental parameters of the CONUS+ experiment used in the statistical analysis. The data correspond to the first direct observation of coherent elastic antineutrino–nucleus scattering (CE ν N/S) [7].

Parameter	Value
<i>Detector system</i>	
Thresholds (C3/C5/C2)	160/170/180 eV _{ee}
Active mass (C2/C3/C5)	0.95/0.94/0.94 kg
Exposure (C2/C3/C5)	117/110/119 days
<i>Antineutrino source</i>	
Antineutrino flux at the detector	$1.5 \times 10^{13} \text{ cm}^{-2}\text{s}^{-1}$
Thermal power P_{th}	3.6 GW
Fission fractions ($^{235}\text{U}/^{238}\text{U}/^{239}\text{Pu}/^{241}\text{Pu}$)	53/8/32/7 %
<i>Observational result</i>	
CE ν N/S events (measured / SM)	$(395 \pm 106)/(347 \pm 59)$
Data/prediction ratio	1.14 ± 0.36
Total uncertainty in SM prediction	17%

terms of $T_{\mathcal{N}}$, the event rate is computed in this variable and mapped to the observable through the detector response function. Accordingly, the differential event rate is written as

$$\frac{dR}{dE_{\text{ee}}^{\text{reco}}} = \mathcal{E} \int_{T_{\mathcal{N}}^{\text{min}}}^{T_{\mathcal{N}}^{\text{max}}} dT_{\mathcal{N}} \mathcal{F}(T_{\mathcal{N}}) \mathcal{G}(E_{\text{ee}}^{\text{reco}}, T_{\mathcal{N}}) \times \int_{E_{\nu}^{\text{min}}(T_{\mathcal{N}})}^{E_{\nu}^{\text{max}}} dE_{\nu} \frac{d\Phi}{dE_{\nu}} \frac{d\sigma}{dT_{\mathcal{N}}}, \quad (29)$$

where \mathcal{E} denotes the detector exposure, defined as the product of the effective data-taking time and the number of target nuclei contained in the active detector volume. In the present implementation, the detection efficiency is taken to be effectively unity within the integration domain, in accordance with the CONUS specifications [7], which report an efficiency $\mathcal{F}(T_{\mathcal{N}})$ close to 100% above the experimental threshold.

The detector response function \mathcal{G} accounts for the stochastic mapping between the nuclear recoil energy and the reconstructed ionization signal and is modeled as a Gaussian distribution centered at the mean ionization energy [9, 38].

$$\mathcal{G}(E_{\text{ee}}^{\text{reco}}, T_{\mathcal{N}}) = \frac{1}{\sqrt{2\pi} \sigma_{\text{res}}(T_{\mathcal{N}})} \exp \left[-\frac{(E_{\text{ee}}^{\text{reco}} - E_{\text{er}}(T_{\mathcal{N}}))^2}{2\sigma_{\text{res}}^2(T_{\mathcal{N}})} \right]. \quad (30)$$

The energy resolution is parameterized as

$$\sigma_{\text{res}}(T_{\mathcal{N}}) = \sqrt{\sigma_0^2 + F_{\text{Fano}} \eta E_{\text{er}}(T_{\mathcal{N}})}, \quad (31)$$

where $\sigma_0 = 20.38 \text{ eV}_{\text{ee}}$, $F_{\text{Fano}} = 0.1096$, and $\eta = 2.96 \text{ eV}_{\text{ee}}$ for germanium detectors [7, 39].

The mean ionization energy E_{er} is related to the nuclear recoil energy $T_{\mathcal{N}}$ through the Lindhard quenching factor,

$$E_{\text{er}}(T_{\mathcal{N}}) = Q_F(T_{\mathcal{N}}) T_{\mathcal{N}}, \quad (32)$$

where the recoil energy $T_{\mathcal{N}}$ should be introduced in eV units. The quenching factor is given by [40, 41]

$$Q_F(T_{\mathcal{N}}) = \frac{k g(\epsilon)}{1 + k g(\epsilon)}, \quad k = 0.162, \quad (33)$$

with $g(\epsilon) = 3\epsilon^{0.15} + 0.7\epsilon^{0.6} + \epsilon$ and $\epsilon = 11.5 Z^{-7/3} T_{\mathcal{N}} \times 10^3$.

The integration limits are determined by detector thresholds and kinematics. The minimum recoil energy $T_{\mathcal{N}}^{\min}$ is obtained by solving $E_{\text{cr}}(T_{\mathcal{N}}^{\min}) = E_{\text{cr}}^{\min}$, where $E_{\text{cr}}^{\min} = 2.96$ eV_{ee} is the detector threshold. This procedure ensures that only recoil events that produce a detectable ionization signal contribute to the event rate, effectively incorporating the detector efficiency over the kinematic integration domain. Therefore, $T_{\mathcal{N}}^{\min} = 2.72 \times 10^{-5}$ MeV.

The maximum recoil energy is fixed by kinematics as

$$T_{\mathcal{N}}^{\max} = \frac{2(E_{\nu}^{\max})^2}{m_{\mathcal{N}} + 2E_{\nu}^{\max}}, \quad (34)$$

the minimum neutrino energy required to produce a recoil $T_{\mathcal{N}}$ is given by

$$E_{\nu}^{\min}(T_{\mathcal{N}}) = \frac{T_{\mathcal{N}}}{2} + \sqrt{\left(\frac{T_{\mathcal{N}}}{2}\right)^2 + \frac{m_{\mathcal{N}} T_{\mathcal{N}}}{2}}, \quad (35)$$

while the upper limit is fixed to $E_{\nu}^{\max} = 10$ MeV.

The reactor antineutrino flux is modeled as a superposition of the contributions from the dominant fissile isotopes $l = \{^{235}\text{U}, ^{238}\text{U}, ^{239}\text{Pu}, ^{241}\text{Pu}\}$ [7]. The differential flux at the detector is written as

$$\frac{d\Phi}{dE_{\nu}}(E_{\nu}, t) = \frac{P_{\text{th}}(t)}{4\pi L^2 \sum_l f_l(t) E_l^{\text{fis}}} \sum_l f_l(t) \lambda_l(E_{\nu}). \quad (36)$$

Here P_{th} is the reactor thermal power, L is the reactor–detector baseline, f_l are the fission fractions, E_l^{fis} are the energies released per fission, and $\lambda_l(E_{\nu})$ is the antineutrino spectrum per fission reported in Ref. [42, 43]. The numerical inputs adopted in this work are listed in Table IV. For the time-integrated CONUS+ dataset, P_{th} and f_l are treated as effective constants.

For neutrino energies above 2 MeV, we followed Ref. [44], where each isotopic spectrum is described by a phenomenological parameterization,

$$\lambda_l(E_{\nu}) = \exp\left[\sum_{k=1}^6 \alpha_{lk} E_{\nu}^{k-1}\right]. \quad (37)$$

The coefficients α_{lk} are obtained from a fit to the converted β -spectra using the MIGRAD minimization algorithm within the TMinuit framework.² The central values of the coefficients α_{lk} reported in Ref. [42, 44] are adopted, and their correlations are neglected. For neutrino energies below 2 MeV, we considered Ref. [45]

To constrain new-physics parameters $\vec{\beta}$ (NSI couplings $\varepsilon_{\alpha\beta}^{qP}$, mediator mass $M_{Z'}$, or coupling $g_{Z'}$), a binned χ^2 function is constructed:

$$\chi^2(\vec{\beta}) = \sum_{i=1}^{19} \frac{[R_i^{\text{exp}} - (1 + \alpha) R_i^{\text{th}}(\vec{\beta})]^2}{\sigma_i^2} + \left(\frac{\alpha}{\sigma_{\alpha}}\right)^2, \quad (38)$$

² The neutrino energy E_{ν} is expressed in MeV in the above parametrization.

where R_i^{exp} is the observed count in bin i , R_i^{th} is the theoretical prediction, σ_i is the statistical uncertainty, and α is a nuisance parameter encoding the overall normalization systematic uncertainty with prior σ_α . The χ^2 is profiled over α analytically for each parameter-space point. Confidence regions are then extracted using

$$\Delta\chi^2 = \chi^2 - \chi_{\min}^2, \quad (39)$$

with Wilks-theorem thresholds: $\Delta\chi^2 = 1.00, 4.00, 9.00$ for $1\sigma, 2\sigma, 3\sigma$ in the one-parameter case, and $\Delta\chi^2 = 2.30, 6.18, 11.83$ for the two-parameter case.

Systematic uncertainties associated with the quenching factor Q_F and the weak nuclear form factor F_W are included in the $\text{CE}\nu\mathcal{N}\text{S}$ signal prediction. The global normalization uncertainty is $\sigma_\alpha = 16.9\%$, with contributions from flux (4.6%), quenching (7.3%), threshold (14.1%), active mass (1.1%), trigger efficiency (0.7%), and weak form factor (3.2%) [7].

IV. ANALYSIS AND RESULTS

In this section, we present the main results of our analysis. First, we analyze the compatibility between CONUS+ data and the theoretical predictions considered in this study through a bin-by-bin pull study. Then, we use the CONUS+ $\text{CE}\nu\mathcal{N}\text{S}$ data to constrain BSM scenarios such as neutrino nonstandard interactions, E_6 -motivated Z' models, and the leptophilic $L_e - L_\mu$ scenario.

A. Analysis of Pulls

The bin-by-bin pulls provide a quantitative measure of the agreement between the experimental data and the theoretical predictions under different hypotheses. Here we compare the SM with extensions including NSI, E_6 -motivated Z' scenarios, and the leptophilic $L_e - L_\mu$ model, using pull morphology and global fit indicators.

To interpret [Figure 2](#), we define the pull in each bin as

$$p_i = \frac{R_i^{\text{exp}} - (1 + \alpha)R_i^{\text{th}}}{\sigma_i}, \quad (40)$$

so that ($p_i > 0 \vee p_i < 0$) indicates that the experimental point lies (above \vee below) the profiled theoretical prediction. With this convention, the lower panel of [Figure 2](#) shows a clear but mild structure: bins 2–4 are predominantly positive, bins 5–13 fluctuate around zero, bins 1, 14–18 are mostly negative, and bin 19 returns to a positive value. This behavior is fully consistent with the visual inspection of the upper panel.

Table V. Global fit statistics for the SM, NSI, E_6 , and $L_e - L_\mu$ models.

Model	\sum Pulls	χ_{\min}^2	χ_{\min}^2/dof	dof
SM	-1.8169	7.3988	0.4110	18
NSI	-2.3947	7.3526	0.5252	14
E_6	-2.3946	7.3526	0.5252	14
$L_e - L_\mu$	-2.4054	7.3494	0.4593	16

The global statistics in [Table V](#) should be interpreted together with the pull morphology in [Figure 2](#): most bins satisfy $|p_i| \lesssim 1$, with the largest deviations concentrated in bins 14, 16, and

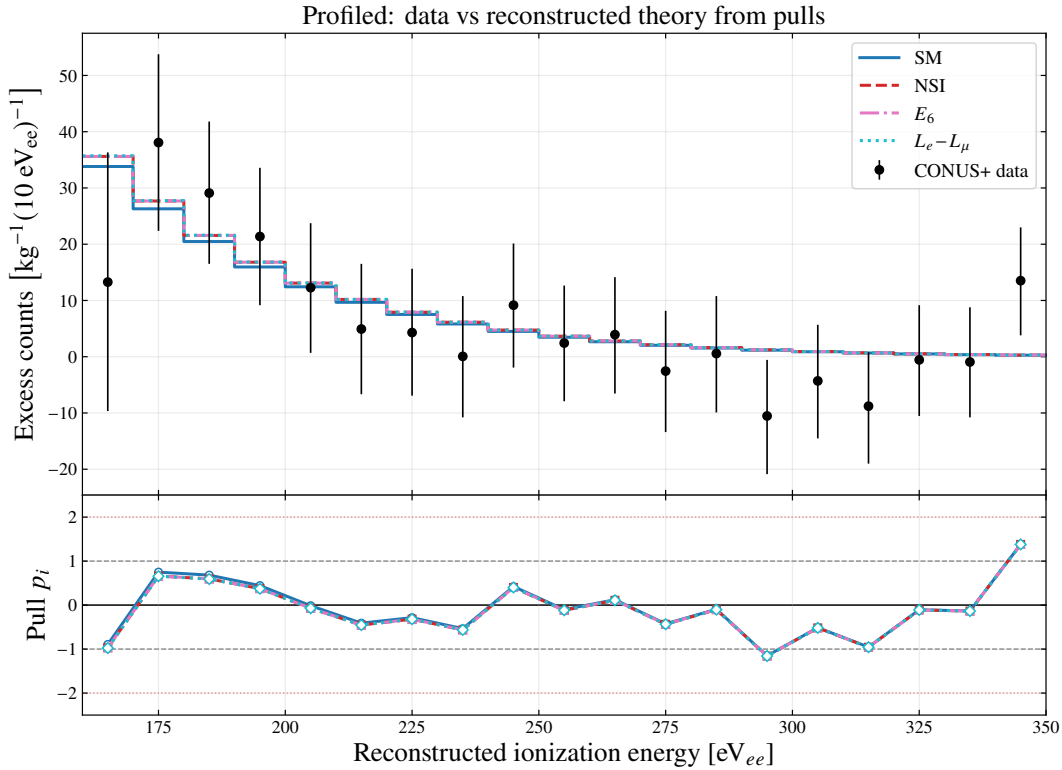


Figure 2. Bin-by-bin pulls for the profiled models in the CONUS+ CE ν NS analysis. [7]

19 at the level of $|p_i| \sim 1.0$ – 1.36 . At the level of absolute minimum, NSI and E_6 improve only marginally with respect to SM ($\chi_{\min}^2 = 7.3526$ vs 7.3988 , i.e. $\Delta\chi^2 \simeq 0.046$), while $L_e - L_\mu$ gives the lowest value ($\chi_{\min}^2 = 7.3494$), still with a very small gain over SM ($\Delta\chi^2 \simeq 0.049$). This marginal variation indicates that the data do not show a statistically meaningful preference for a BSM hypothesis.

From a goodness-of-fit perspective that also accounts for model complexity, the comparison in χ_{\min}^2/dof is instructive: SM gives 0.4110 , $L_e - L_\mu$ gives 0.4593 , and NSI/ E_6 gives 0.5252 . Since the reduction in χ_{\min}^2 is negligible, but the number of fitted parameters increases (smaller dof), the more complex models do not provide a commensurate gain in descriptive power. Therefore, under a parsimony criterion, the SM remains the preferred benchmark for the CONUS+ pull dataset, while BSM scenarios should be interpreted as compatible alternatives rather than statistically favored explanations.

From the physics standpoint, the sign structure of the pulls is also informative. Negative pulls in the high-energy tail indicate that the corresponding profiled prediction is locally above the measured excess, whereas positive pulls in the lowest and final bins indicate local underprediction. Since this alternation does not develop into a coherent, same-sign trend across the full spectrum and the magnitudes remain at the $\mathcal{O}(1\sigma)$ level, the observed residuals are better interpreted as localized shape tensions and statistical fluctuations than as evidence for a new interaction component.

B. Neutrino Non-Standard Interactions

Possible deviations from the SM prediction are investigated through a dedicated analysis of NSI. In this framework, new-physics effects are parametrized by the effective vector couplings $\varepsilon_{\alpha\beta}^{qV}$, which modify the coherent nuclear vector charge and hence the CE ν NS cross section, as described in [section II B](#). The CONUS+ dataset is analyzed both in the one-parameter and two-parameter configurations, providing complementary information on the structure of the allowed region in parameter space. The one-dimensional $\Delta\chi^2$ profiles for each of the four independent NSI parameters are shown in [Figure 3](#), while the two-dimensional joint confidence regions for all possible pairings are presented in [Figure 4](#).

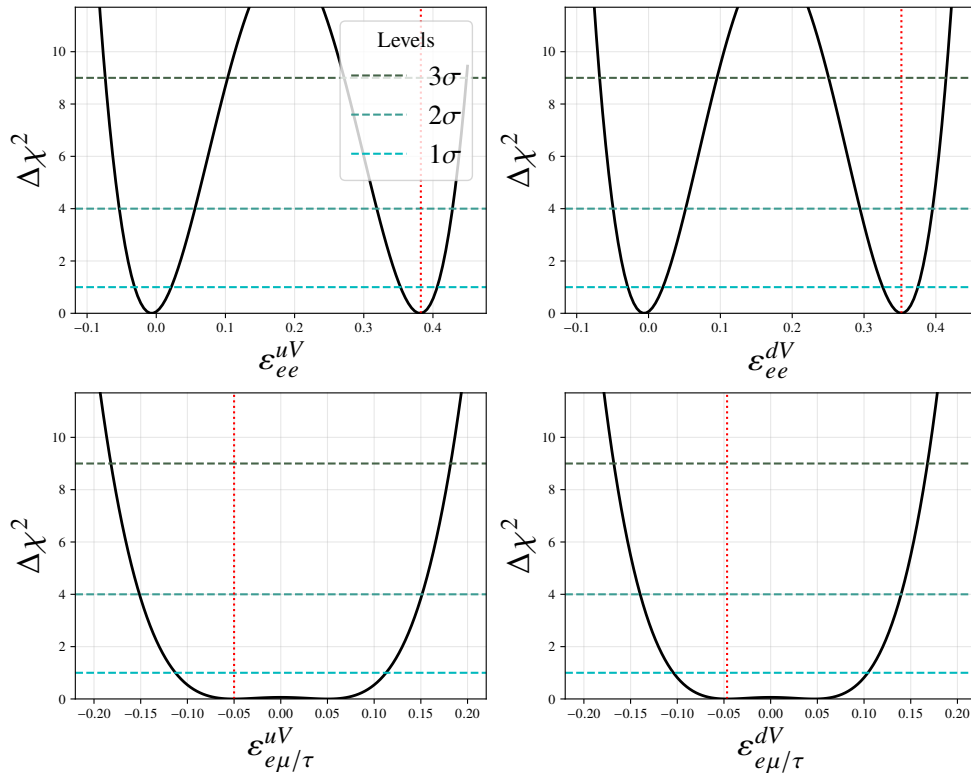


Figure 3. One-dimensional $\Delta\chi^2$ profiles for individual vector NSI parameters $\varepsilon_{\alpha\beta}^{qV}$ obtained from the CONUS+ CE ν NS analysis. Each parameter is varied independently while profiling over the nuisance parameter α . The black, green, and blue dashed horizontal lines indicate the 3σ , 2σ , and 1σ confidence thresholds ($\Delta\chi^2 = 9.00, 4.00, 1.00$), respectively. The red vertical line marks the best-fit point for each parameter. The SM corresponds to $\varepsilon_{\alpha\beta}^{qV} = 0$.

In [Figure 3](#), the diagonal parameters ε_{ee}^{uV} and ε_{ee}^{dV} exhibit a qualitatively distinct behavior: their $\Delta\chi^2$ profiles display two separate local minima, one in the vicinity of the SM limit ($\varepsilon_{ee}^{qV} \approx 0$) and a second degenerate solution near $\varepsilon_{ee}^{qV} \sim 0.35\text{--}0.41$. This double-minimum structure is a direct consequence of the quadratic character of $(Q_V^{\text{NSI}})^2$ (see [section II B](#)): the diagonal NSI parameters enter the weak charge through a linear shift of the SM vector couplings, so the squared amplitude admits two distinct parameter values that yield the same predicted event rate. At an intermediate value between the two minima, there exists a local maximum, which acts as a barrier in the $\Delta\chi^2$ landscape and produces a disconnected confidence region.

The flavor-changing parameters $\varepsilon_{e\mu/\tau}^{uV}$ and $\varepsilon_{e\mu/\tau}^{dV}$, by contrast, contribute only incoherently to the

nuclear scattering amplitude — they enter $(Q_V^{\text{NSI}})^2$ as an additive positive-definite sum, without any interference with the SM contribution. As a result, their $\Delta\chi^2$ profiles present a single broad minimum around $\varepsilon_{e\mu/\tau}^{qV} = 0$, with a flat-bottomed parabolic shape that rises sharply only for $|\varepsilon_{e\mu/\tau}^{qV}| \gtrsim 0.5$. The absence of a secondary critical point implies that each confidence region is a single connected interval, symmetric about zero. The plateau region around $\varepsilon_{e\mu/\tau}^{qV} = 0$ is physically meaningful: it indicates that the data are fully consistent with the absence of lepton-flavor-changing neutral currents in the neutrino sector and that no off-diagonal NSI beyond the SM is required to describe the CONUS+ measurement.

The numerical 1σ confidence intervals extracted from the one-dimensional profiles are summarized in Table VI. We compare our results with the independent CONUS+ analysis of Ref. [8]. For completeness, we also include the COHERENT CsI+LAr bounds quoted in Ref. [46], which provide a direct CE ν NS benchmark based on a different neutrino source and target composition.

Table VI. 1σ confidence intervals for vector NSI parameters obtained from the CONUS+ analysis.

Parameter	This work	CONUS+ [8]	COHERENT CsI+LAr [46]
ε_{ee}^{uV}	$[-0.0381, 0.0251] \cup [0.3497, 0.4128]$	$[-0.037, 0.026] \cup [0.348, 0.411]$	$[-0.024, 0.045] \cup [0.34, 0.43]$
ε_{ee}^{dV}	$[-0.0351, 0.0234] \cup [0.3226, 0.3811]$	$[-0.034, 0.024] \cup [0.322, 0.380]$	$[-0.027, 0.048] \cup [0.30, 0.39]$
$\varepsilon_{e\mu/\tau}^{uV}$	$[-0.1250, 0.1250]$	$[-0.123, 0.123]$	$e\mu : [-0.081, 0.081]$ $e\tau : [-0.13, 0.13]$
$\varepsilon_{e\mu/\tau}^{dV}$	$[-0.1155, 0.1154]$	$[-0.114, 0.114]$	$e\mu : [-0.071, 0.071]$ $e\tau : [-0.12, 0.12]$

The agreement between the first two columns of Table VI validates the present numerical implementation against the independent CONUS+ analysis of Ref. [8]. The small residual differences can be attributed to numerical implementation choices, including the treatment of the weak nuclear form factor, here approximated as $F_W \simeq 1$, and to differences in the integration grid and interpolation strategy. In both analyses, the SM point $\varepsilon_{\alpha\beta}^{qV} = 0$ lies within the 1σ confidence regions.

The comparison with COHERENT should be understood as a direct CE ν NS comparison, but not as a one-to-one replication of the same experimental conditions. CONUS+ uses reactor $\bar{\nu}_e$ and a germanium target, whereas COHERENT uses stopped-pion neutrinos and CsI+LAr targets. The different proton-to-neutron ratios modify the degeneracy directions in the NSI parameter space, while the different flavor composition explains why COHERENT distinguishes $\varepsilon_{e\mu}^{qV}$ from $\varepsilon_{e\tau}^{qV}$. Numerically, CONUS+ provides constraints comparable to COHERENT in the flavor-preserving sector and is competitive in the $e\tau$ flavor-changing sector, while COHERENT remains stronger for the $e\mu$ flavor-changing parameters due to its sizeable ν_μ component.

Although the one-parameter analysis provides useful bounds for individual NSI couplings, it does not capture the correlations among them. Thus, we extend the analysis to two-parameter fits, varying pairs of NSI coefficients simultaneously while profiling over the nuisance parameter α .

The two-dimensional regions in Figure 4 complement the one-dimensional profiles and make the structure of the NSI degeneracies explicit. In the flavor-preserving plane $(\varepsilon_{ee}^{uV}, \varepsilon_{ee}^{dV})$, the allowed region is organized into two approximately parallel bands. These bands are the two-dimensional manifestation of the two one-dimensional minima discussed above: one branch is connected with the SM solution, while the second branch corresponds to the non-SM solution generated by the sign degeneracy of the effective weak charge.

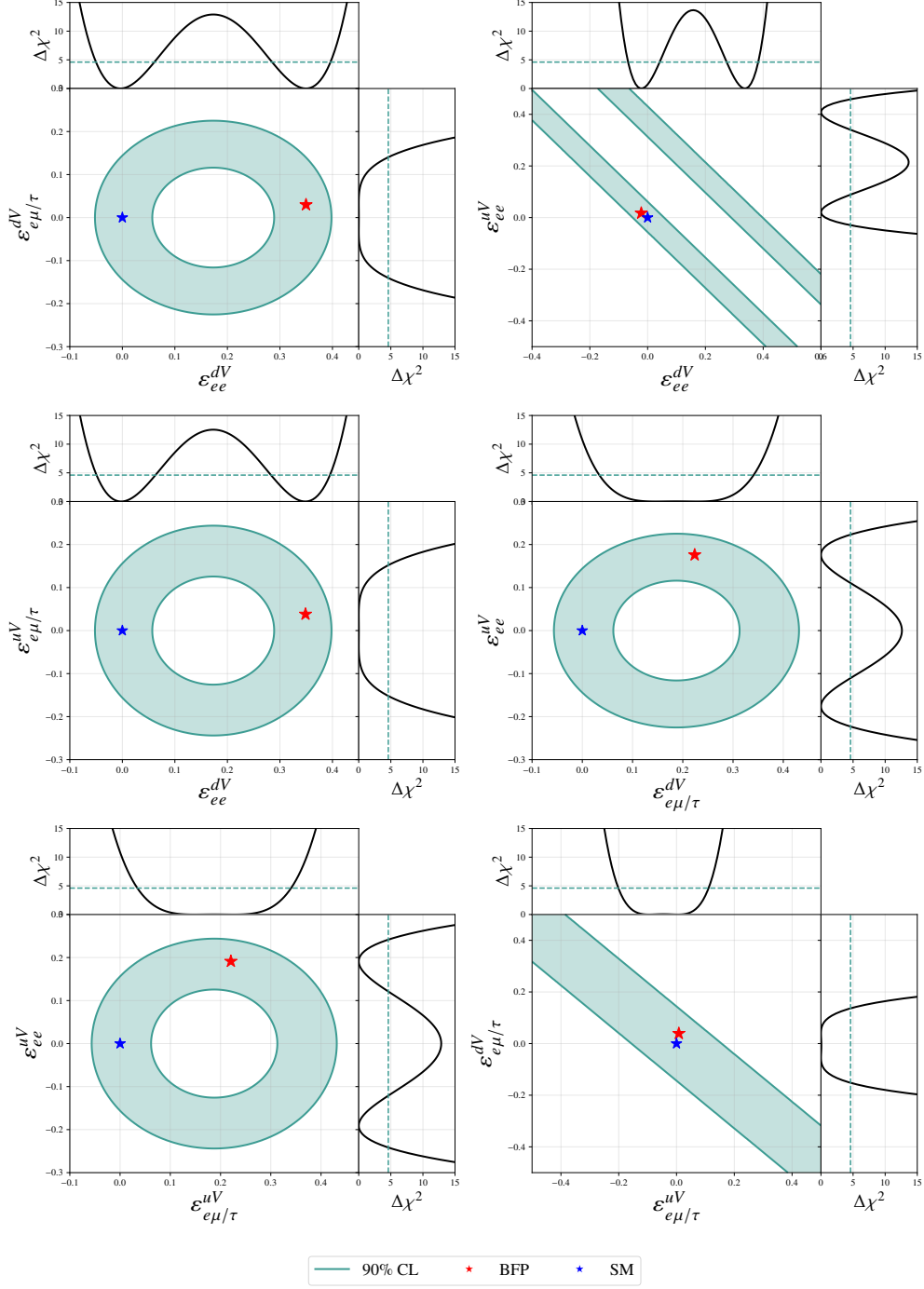


Figure 4. Two-dimensional confidence regions at 90% CL for all pairings of the vector NSI parameters $\varepsilon_{\alpha\beta}^{qV}$, obtained from the profiled $\Delta\chi^2$ with two degrees of freedom. The SM prediction, $\varepsilon_{\alpha\beta}^{qV} = 0$, lies at the origin of each panel.

In the flavor-changing plane $(\varepsilon_{e\mu/\tau}^{uV}, \varepsilon_{e\mu/\tau}^{dV})$, the allowed region forms a single open band. This follows directly from the fact that flavor-changing NSI enter the $\text{CE}\nu\mathcal{N}\text{S}$ rate only through the squared linear combination

$$\left[Z \left(2\varepsilon_{e\mu/\tau}^{uV} + \varepsilon_{e\mu/\tau}^{dV} \right) + N \left(\varepsilon_{e\mu/\tau}^{uV} + 2\varepsilon_{e\mu/\tau}^{dV} \right) \right]^2. \quad (41)$$

The two planes $(\varepsilon_{ee}^{uV}, \varepsilon_{ee}^{dV})$ and $(\varepsilon_{e\mu/\tau}^{uV}, \varepsilon_{e\mu/\tau}^{dV})$ exhibit open degeneracy bands because the CE ν N S rate constrains only specific linear combinations of the corresponding NSI couplings. Consequently, finite independent bounds cannot be extracted from these planes alone. By contrast, the four mixed parameter planes display closed confidence regions, where the interplay between the flavor-preserving and flavor-changing contributions confines the allowed parameter space around the best-fit solutions. In every panel, the SM point lies inside the allowed region, showing that the CONUS+ data remain fully consistent with the absence of NSI.

At the contour level, the topology of the two-dimensional regions agrees with the behavior reported in Ref. [8] for CONUS+ and with previous COHERENT CE ν N S analyses. The most relevant comparison with COHERENT is not a direct comparison of one-dimensional projections, but rather the complementarity of the two-dimensional bands. Because germanium, CsI, and argon have different proton-to-neutron ratios, the allowed bands in the $(\varepsilon_{ee}^{dV}, \varepsilon_{ee}^{uV})$ and $(\varepsilon_{e\mu/\tau}^{dV}, \varepsilon_{e\mu/\tau}^{uV})$ planes have different slopes. This complementarity is essential for breaking CE ν N S degeneracies in combined multi-target analyses.

The 90% C.L. one-dimensional projections extracted from the two-parameter regions are summarized in Table VII. These intervals are projections of the two-dimensional confidence regions, not independent one-parameter bounds. For the two planes with analytical degeneracy directions, the projections are reported as unbounded.

Table VII. One-dimensional projections of the 90% C.L. two-parameter NSI confidence regions obtained from the CONUS+ CE ν N S analysis. Closed regions lead to finite projections, while open degeneracy bands are reported as unbounded. The intervals are projections of the corresponding two-dimensional regions and should not be interpreted as independent one-parameter fits.

Two-parameter plane	First-axis projection	Second-axis projection	Topology
$(\varepsilon_{ee}^{dV}, \varepsilon_{e\mu/\tau}^{dV})$	$\varepsilon_{ee}^{dV} \in [-0.050, 0.395]$	$ \varepsilon_{e\mu/\tau}^{dV} < 0.225$	Closed
$(\varepsilon_{ee}^{dV}, \varepsilon_{ee}^{uV})$	Unbounded	Unbounded	Open degeneracy band
$(\varepsilon_{ee}^{dV}, \varepsilon_{e\mu/\tau}^{uV})$	$\varepsilon_{ee}^{dV} \in [-0.050, 0.395]$	$ \varepsilon_{e\mu/\tau}^{uV} < 0.240$	Closed
$(\varepsilon_{ee}^{uV}, \varepsilon_{e\mu/\tau}^{dV})$	$\varepsilon_{ee}^{uV} \in [-0.052, 0.427]$	$ \varepsilon_{e\mu/\tau}^{dV} < 0.225$	Closed
$(\varepsilon_{ee}^{uV}, \varepsilon_{e\mu/\tau}^{uV})$	$\varepsilon_{ee}^{uV} \in [-0.052, 0.427]$	$ \varepsilon_{e\mu/\tau}^{uV} < 0.240$	Closed
$(\varepsilon_{e\mu/\tau}^{uV}, \varepsilon_{e\mu/\tau}^{dV})$	Unbounded	Unbounded	Open degeneracy band

The unbounded entries in Table VII have a clear physical origin. They correspond to two-parameter planes in which the CONUS+ germanium target constrains only one effective linear combination of the two NSI couplings. As a result, the allowed region extends along a line in parameter space and cannot be converted into finite individual bounds without additional information.

For the closed mixed regions, the projected limits are finite and numerically coincide with the maximal ranges obtained from the two-dimensional contours. The projections show that the flavor-preserving parameters are allowed over the intervals

$$\varepsilon_{ee}^{dV} \in [-0.050, 0.395], \quad \varepsilon_{ee}^{uV} \in [-0.052, 0.427], \quad (42)$$

while the flavor-changing parameters satisfy

$$|\varepsilon_{e\mu/\tau}^{dV}| < 0.225, \quad |\varepsilon_{e\mu/\tau}^{uV}| < 0.240. \quad (43)$$

These values summarize the finite extent of the closed two-dimensional regions. However, they should be interpreted with caution because a projection only states that, for a given value of

one parameter, there exists at least one value of the second parameter that lies inside the two-dimensional confidence region. It does not imply that all values of the second parameter are allowed.

At the two-dimensional level, the comparison with COHERENT is therefore mainly one of complementarity rather than a direct comparison of projected intervals. CONUS+, COHERENT-CsI, and COHERENT-LAr have different proton-to-neutron ratios, so their $\text{CE}\nu\mathcal{NS}$ degeneracy directions in the $(\varepsilon^{uV}, \varepsilon^{dV})$ planes have different slopes.

C. Neutrino Generalized Interactions via a Light Z'

1. E_6 Models

Grand-unified extensions based on groups such as E_6 predict additional neutral gauge bosons (Z'). In the SF basis, the model dependence is encoded in the angular parameters (α, β) , which select the benchmark direction in the E_6 parameter space. For the numerical analysis, we adopt the conventional unification-motivated normalization $g_{Z'} = 0.46$, following the normalization used in Ref. [31].

The allowed regions in the (α, β) plane for six representative Z' masses are shown in Figure 5. The main trend is clear: for light mediators, the excluded part of the parameter space is larger, while the allowed region becomes progressively broader as the Z' mass increases. This behavior follows from the propagator suppression of the new contribution to $\text{CE}\nu\mathcal{NS}$: when $m_{Z'}$ becomes large compared with the typical momentum transfer, the effect of the new boson on the recoil spectrum decreases. In the largest-mass panels, the contours nearly saturate the scanned domain, indicating that the present CONUS+ dataset loses sensitivity to the angular structure of the E_6 benchmarks in that regime.

The benchmark directions listed in Table II provide a useful interpretation of this pattern. In general, configurations that suppress either the effective neutrino coupling or the coherent nuclear vector charge are less efficiently constrained, whereas benchmark points with stronger effective couplings are more readily excluded by the data.

A complementary view is given in Figure 6, where the results are displayed directly in the $(m_{Z'}, g_{Z'})$ plane. Panel (a) of Figure 6 shows the exclusion envelopes for the benchmark E_6 models of Table II, while panel (b) of Figure 6 shows the corresponding exclusion region for the leptophilic $L_e - L_\mu$ scenario discussed below. In both cases, the exclusion contours display the characteristic behavior of a light vector mediator. In the low-mass regime, $m_{Z'}^2 \ll |q^2|$, the propagator is dominated by the momentum transfer, and the dependence on the mediator mass becomes weak. As a result, the exclusion boundary approaches an approximately constant value, producing a horizontal low-mass plateau. Conversely, for $m_{Z'}^2 \gg |q^2|$, the propagator suppresses the new-physics contribution, and increasingly larger values of $g_{Z'}$ are required to generate an observable distortion of the recoil spectrum. The loss of sensitivity at large mediator masses is therefore a common feature of both the E_6 and leptophilic scenarios.

For the E_6 benchmarks, the separation among the exclusion envelopes is mainly driven by the different charge assignments. The relevant scaling is controlled by the effective product $g_V^{Z'}(\nu)Q_{N,V}^{Z'}$ entering the $\text{CE}\nu\mathcal{NS}$ amplitude. Benchmarks with larger effective products generate larger spectral distortions for the same value of $g_{Z'}$ and are therefore constrained at smaller couplings. Conversely, benchmarks with suppressed effective charges or partial cancellations require larger couplings to reach the same statistical exclusion threshold.

The corresponding low-mass plateau values, extracted from the numerical scan, are summarized in Table VIII. The quantity $g_{Z'}^{\text{lim}}$ represents the approximately constant upper limit in the

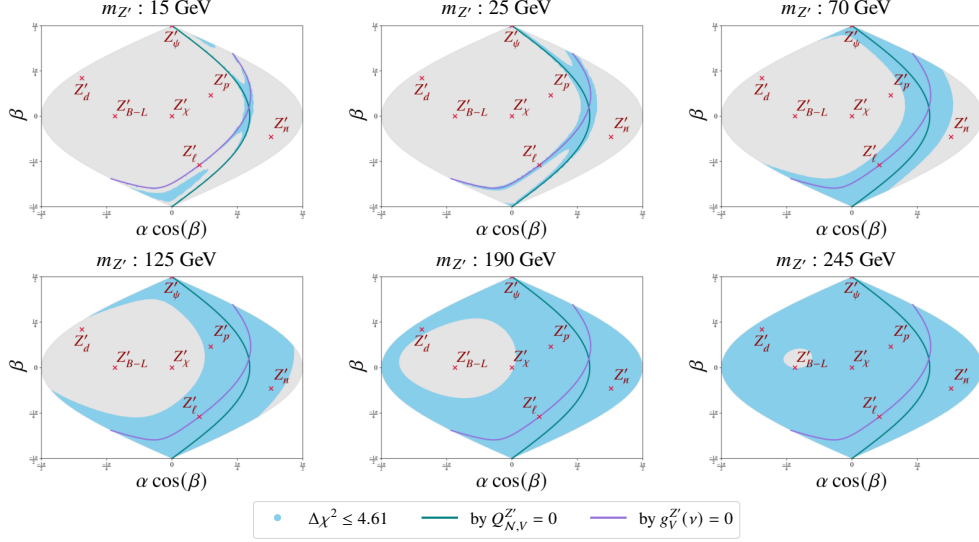


Figure 5. Allowed regions in the SF E_6 parameter space (α, β) for six representative Z' masses, obtained with the canonical normalization $g_{Z'} = \sqrt{5/3} g \tan \theta_W \simeq 0.46$ [31]. Each panel displays the configurations compatible with the CONUS+ data at 90% confidence level for two degrees of freedom. The constraints are strongest for the lightest mediator masses and become progressively weaker as the mass increases, until the scanned region is nearly unconstrained for the largest values of $m_{Z'}$. The angular parameters span $\alpha, \beta \in [-\pi/2, \pi/2]$. Benchmark cases are listed in Table II.

light-mediator regime, while the quoted mass range indicates the interval over which the exclusion boundary remains compatible with the initial flat segment.

Table VIII. Low-mass plateau of the 90% C.L. exclusion boundaries for the benchmark E_6 models in the $(m_{Z'}, g_{Z'})$ plane. The quantity $g_{Z'}^{\text{lim}}$ denotes the approximately constant upper limit in the regime $m_{Z'}^2 \ll q^2$, where the sensitivity is nearly independent of the mediator mass. The third column gives the approximate upper bound of this regime, corresponding to the point at which $m_{Z'}$ becomes comparable to the characteristic momentum-transfer scale probed by CONUS+ and the exclusion contour begins to rise.

Benchmark model	$g_{Z'}^{\text{lim}}$	Low-mass plateau range
Z'_{B-L}	2.19×10^{-5}	$m_{Z'} \lesssim 4.07 \text{ MeV}$
Z'_{χ}	2.69×10^{-5}	$m_{Z'} \lesssim 3.09 \text{ MeV}$
Z'_{ψ}	3.09×10^{-5}	$m_{Z'} \lesssim 3.55 \text{ MeV}$
Z'_{η}	5.37×10^{-5}	$m_{Z'} \lesssim 1.35 \text{ MeV}$
Z'_{ϕ}	5.01×10^{-5}	$m_{Z'} \lesssim 3.80 \text{ MeV}$

The strongest low-mass constraint is obtained for Z'_{B-L} , with

$$g_{Z'}^{\text{lim}} = 2.19 \times 10^{-5}$$

for $m_{Z'} \lesssim 4.07 \text{ MeV}$. This result is consistent with the evolution of $\text{CE}\nu\mathcal{N}\mathcal{S}$ bounds on $U(1)_{B-L}$ vector mediators reported in the literature. Earlier analyses based on COHERENT data typically reached sensitivities of order 10^{-4} – 10^{-3} for MeV-scale mediators [19, 47], whereas reactor-based measurements with CONUS and the first CONUS+ result have pushed the sensitivity into the 10^{-5} regime [8, 12]. The present $B-L$ plateau therefore lies within the expected range of modern low-threshold reactor $\text{CE}\nu\mathcal{N}\mathcal{S}$ constraints.

It is followed by Z'_χ and Z'_ϕ , whose plateau limits are 2.69×10^{-5} for $m_{Z'} \lesssim 3.09 \text{ MeV}$ and 3.09×10^{-5} for $m_{Z'} \lesssim 3.55 \text{ MeV}$, respectively. The weakest low-mass bounds correspond to Z'_β and Z'_η , with plateau values around 5×10^{-5} . This ordering should not be interpreted as a statistical preference for one benchmark over another; rather, it is a consequence of the different combinations of $g_V^{Z'}(\nu)$ and $Q_{N,V}^{Z'}$ entering the $\text{CE}\nu\text{NS}$ amplitude. Unlike the $B-L$ case, dedicated $\text{CE}\nu\text{NS}$ limits for the other benchmark directions are not commonly available in the literature. The present analysis therefore extends the CONUS+ sensitivity study to a broader class of E_6 -motivated scenarios.

For mediator masses above the corresponding plateau range, the exclusion envelopes begin to rise. At the upper edge of the scan, $m_{Z'} = 10^4 \text{ MeV}$, the exclusion boundary has already moved to much larger couplings, reaching values between $g_{Z'} \simeq 1.78 \times 10^{-2}$ for Z'_{B-L} and $g_{Z'} \simeq 4.68 \times 10^{-2}$ for Z'_η . Panel (a) of [Figure 6](#) should therefore be read as a benchmark-dependent translation of the CONUS+ spectral information into exclusion limits on $(m_{Z'}, g_{Z'})$, rather than as evidence for a preferred E_6 realization.

2. Leptophilic models

Alternative generalized interactions can also arise from leptophilic gauge symmetries, such as $L_e - L_\mu$. In this scenario, the new gauge boson Z' couples directly to the electron and muon lepton numbers at tree level, while quarks remain neutral under the new symmetry. Consequently, the interaction with the nuclear target relevant for $\text{CE}\nu\text{NS}$ is not generated by a tree-level coupling to the coherent weak charge, but rather through the loop-induced $A-Z'$ kinetic mixing discussed in the theoretical formalism. This feature makes reactor $\text{CE}\nu\text{NS}$ a complementary probe of the electronic leptophilic sector, since it tests the nuclear-recoil imprint of a gauge interaction that is purely leptonic at tree level.

The exclusion region in the $(m_{Z'}, g_{Z'})$ plane is shown in panel (b) of [Figure 6](#). In this case, the boundary separates the allowed region, shown in blue, from the excluded region, shown in red, at 90% confidence level for two degrees of freedom. The modification of the $\text{CE}\nu\text{NS}$ spectrum is induced through the loop-generated kinetic mixing between the photon and the new gauge boson. Since this kinetic-mixing parameter is proportional to $g_{Z'}$, the leading leptophilic contribution scales approximately as $g_{Z'}^2/(q^2 - m_{Z'}^2)$.

Thus, the same light-mediator behavior described above leads to a low-mass plateau in the leptophilic exclusion curve. From the numerical scan, the exclusion contour remains approximately flat up to $m_{Z'} \simeq 2.51 \text{ MeV}$, yielding the upper bound

$$g_{Z'}^{\text{lim}} = 8.51 \times 10^{-5}. \quad (44)$$

This value should be interpreted as the low-mass plateau of the CONUS+ $\text{CE}\nu\text{NS}$ constraint for the leptophilic $L_e - L_\mu$ model, valid for $m_{Z'} \lesssim 2.51 \text{ MeV}$ within the numerical resolution of the scan. The value $m_{Z'} \simeq 2.51 \text{ MeV}$ does not represent a special physical scale, but only the point at which the numerically identified flat region begins to depart from the plateau. For larger mediator masses, the sensitivity weakens rapidly, and the exclusion boundary reaches approximately $g_{Z'} \simeq 0.72$ at $m_{Z'} = 10^5 \text{ MeV}$.

The comparison with electronic leptophilic probes must be made with care. Solar-neutrino and liquid-xenon electron-recoil analyses constrain $L_e - L_\mu$ through direct leptonic interactions in νe scattering, and their low-mass limits typically reach the level $g_{Z'} \sim 10^{-7}$ for $m_{Z'} \lesssim 10^{-3} \text{ MeV}$ [6, 14–18]. By contrast, in $\text{CE}\nu\text{NS}$ the same leptophilic boson modifies the nuclear recoil spectrum only after the loop-induced mixing with the photon generates an effective coupling to the nuclear electromagnetic current. This loop and channel dependence naturally explains why the CONUS+

plateau obtained here is weaker than the bounds from direct electronic scattering. Its relevance is therefore not in superseding νe limits, but in providing an independent nuclear-recoil constraint on the electronic leptophilic gauge interaction.

Overall, Figure 6 shows that reactor $\text{CE}\nu\mathcal{N}\text{S}$ data retain the expected mediator-mass dependence across both classes of models: a constant exclusion plateau in the light regime, followed by a rapid degradation of sensitivity as the mediator becomes heavy. For the E_6 benchmarks, the differences among curves are driven by the corresponding charge assignments, while for $L_e - L_\mu$ the nuclear response arises only through the loop-induced coupling to the electromagnetic current. In this sense, the CONUS+ data provide a complementary low-energy probe of both quark-coupled and leptophilic light-vector scenarios.

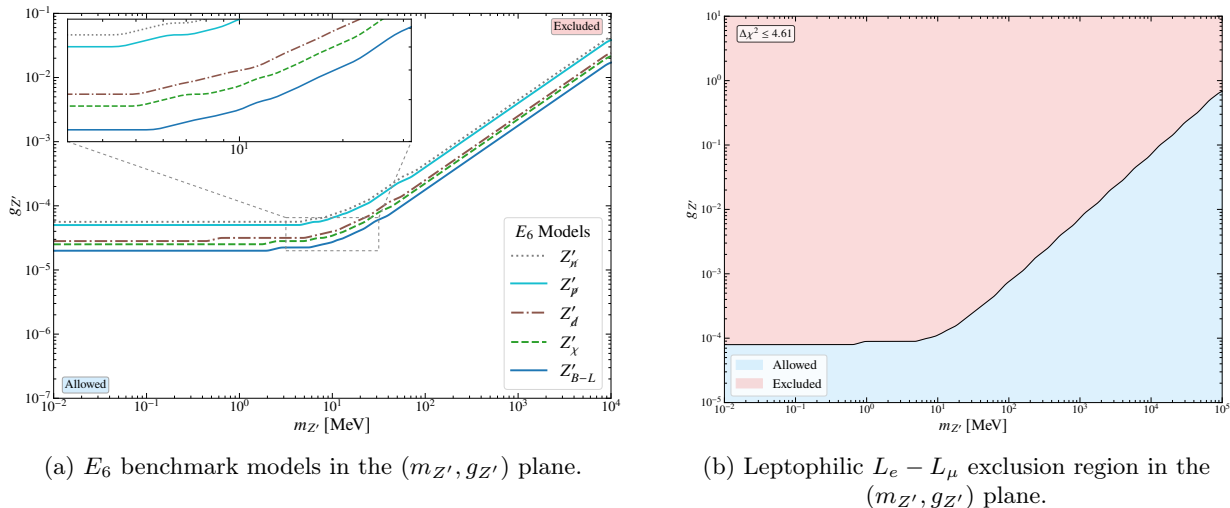


Figure 6. Combined constraints in the $(m_{Z'}, g_{Z'})$ parameter space from the CONUS+ $\text{CE}\nu\mathcal{N}\text{S}$ analysis at 90% C.L. for two degrees of freedom. Panel (a) shows the exclusion envelopes for the benchmark E_6 models of Table II. Panel (b) shows the exclusion region for the leptophilic $L_e - L_\mu$ model, where the blue region is allowed and the red region is excluded. In both cases, the constraints are stronger in the light-mediator regime and weaken as $m_{Z'}$ increases due to propagator suppression.

V. CONCLUSIONS

We have performed a binned- χ^2 analysis of the first CONUS+ measurement of coherent elastic antineutrino–nucleus scattering on germanium. The analysis employs a profiled nuisance-parameter treatment of the global normalization uncertainty, allowing the SM, NSI, E_6 -motivated light- Z' scenarios, and the leptophilic $U(1)_{L_e - L_\mu}$ model to be studied within a common statistical framework.

The CONUS+ data are fully consistent with the SM prediction. The measured excess is compatible with the expected $\text{CE}\nu\mathcal{N}\text{S}$ signal, the pull distribution exhibits no coherent spectral distortion, and the best-fit χ^2 values differ only marginally among the SM and the BSM scenarios considered. After accounting for the number of fitted parameters, the SM remains the most parsimonious description of the present CONUS+ dataset.

In the NSI sector, the one-dimensional analysis reproduces the characteristic $\text{CE}\nu\mathcal{N}\text{S}$ degeneracy pattern. The flavor-preserving parameters exhibit a two-branch structure, reflecting the quadratic dependence of the rate on the effective weak charge, whereas the flavor-changing parameters remain near the SM point. The resulting 1σ confidence intervals are summarized in Table VI, where they

are shown to be in excellent agreement with the independent CONUS+ analysis of Ref. [8]. In all cases, the SM point lies within the allowed region, indicating that the present data constrain NSI couplings but provide no evidence for non-standard neutrino interactions.

The two-dimensional analysis further clarifies the structure of the NSI parameter space. The flavor-preserving and flavor-changing planes exhibit open degeneracy bands, while the mixed planes yield closed confidence regions with finite projections. These projected intervals, reported in Table VII, should be interpreted as projections of two-dimensional confidence regions rather than independent one-parameter bounds. Comparison with COHERENT highlights the complementarity between reactor and stopped-pion $CE\nu\mathcal{N}S$ measurements. The different proton-to-neutron ratios of Ge, CsI, and Ar produce different degeneracy directions in the $(\varepsilon^{uV}, \varepsilon^{dV})$ parameter space, demonstrating that combined multi-target analyses will be essential for improving future NSI constraints.

Within the E_6 framework, the Sanson–Flamsteed analysis provides a geometric interpretation of the CONUS+ sensitivity by identifying the regions of the (α, β) plane that are compatible with the data. Light mediators exclude sizeable portions of the parameter space, while sensitivity decreases progressively with increasing mediator mass due to propagator suppression. The corresponding exclusion limits for the benchmark E_6 models are summarized in Table VIII. Among the scenarios considered, the Z'_{B-L} direction provides the strongest constraints.

For the leptophilic $U(1)_{L_e-L_\mu}$ model, the $CE\nu\mathcal{N}S$ signal arises through loop-induced $A-Z'$ kinetic mixing, which generates an effective coupling to the nuclear electromagnetic current. The resulting exclusion contour exhibits the expected low-mass plateau followed by a rapid loss of sensitivity at larger mediator masses. Although the corresponding bounds are weaker than those obtained from direct neutrino–electron scattering experiments, they constitute an independent and complementary nuclear-recoil probe of the same leptophilic interaction.

Overall, the first CONUS+ $CE\nu\mathcal{N}S$ measurement shows no statistically significant preference for NSI, E_6 -motivated vector mediators, or leptophilic light- Z' scenarios. Instead, it provides competitive constraints on these BSM frameworks while remaining fully consistent with the SM. Future reactor $CE\nu\mathcal{N}S$ measurements with larger exposures, lower detection thresholds, improved quenching-factor calibration, and reduced normalization uncertainties are expected to further strengthen these constraints. In addition, the complementarity observed between CONUS+ and COHERENT suggests that combined analyses of reactor and stopped-pion $CE\nu\mathcal{N}S$ data using multiple nuclear targets constitute a promising strategy for lifting NSI degeneracies and improving the sensitivity to light vector mediators.

ACKNOWLEDGMENTS

This article is derived from a master’s thesis in Applied Statistics at the Universidad de Nariño, Colombia, entitled “*Estimación estadística de regiones de confianza para interacciones no estándar y bosones Z' ligeros a partir de datos $CE\nu\mathcal{N}S$ del experimento CONUS+*”.

Ch.M.B., C.S.M. and E.R. acknowledge the Universidad de Nariño for its academic support during the development of this work, as well as support from the Vicerrectoría de Investigaciones e Interacción Social (VIIS) of the Universidad de Nariño under project numbers 3595 and 3899.

B.C. and E.R. acknowledge support from the Minciencias Grant CD 82315 CT ICETEX 2021-

1080.

-
- [1] Daniel Z. Freedman. Coherent Neutrino Nucleus Scattering as a Probe of the Weak Neutral Current. *Phys. Rev. D*, 9:1389–1392, 1974. doi:10.1103/PhysRevD.9.1389.
- [2] D. Akimov et al. Observation of Coherent Elastic Neutrino-Nucleus Scattering. *Science*, 357(6356):1123–1126, 2017. arXiv:1708.01294, doi:10.1126/science.aao0990.
- [3] D. Akimov et al. First Measurement of Coherent Elastic Neutrino-Nucleus Scattering on Argon. *Phys. Rev. Lett.*, 126(1):012002, 2021. arXiv:2003.10630, doi:10.1103/PhysRevLett.126.012002.
- [4] S. Adamski et al. Evidence of Coherent Elastic Neutrino-Nucleus Scattering with COHERENT’s Germanium Array. *Phys. Rev. Lett.*, 134(23):231801, 2025. arXiv:2406.13806, doi:10.1103/PhysRevLett.134.231801.
- [5] Zihao Bo et al. First Indication of Solar B8 Neutrinos through Coherent Elastic Neutrino-Nucleus Scattering in PandaX-4T. *Phys. Rev. Lett.*, 133(19):191001, 2024. arXiv:2407.10892, doi:10.1103/PhysRevLett.133.191001.
- [6] Elena Aprile et al. First Indication of Solar B8 Neutrinos via Coherent Elastic Neutrino-Nucleus Scattering with XENONnT. *Phys. Rev. Lett.*, 133(19):191002, 2024. arXiv:2408.02877, doi:10.1103/PhysRevLett.133.191002.
- [7] N. Ackermann et al. Direct observation of coherent elastic antineutrino–nucleus scattering. *Nature*, 643(8074):1229–1233, 2025. arXiv:2501.05206, doi:10.1038/s41586-025-09322-2.
- [8] Valentina De Romeri, Dimitrios K. Papoulias, and Gonzalo Sanchez Garcia. Implications of the first CONUS+ measurement of coherent elastic neutrino-nucleus scattering. *Phys. Rev. D*, 111(7):075025, 2025. arXiv:2501.17843, doi:10.1103/PhysRevD.111.075025.
- [9] Ayan Chattaraj, Anirban Majumdar, and Rahul Srivastava. Probing standard model and beyond with reactor CE ν NS data of CONUS+ experiment. *Phys. Lett. B*, 864:139438, 2025. arXiv:2501.12441, doi:10.1016/j.physletb.2025.139438.
- [10] Gail McLaughlin. Theory and phenomenology of coherent neutrino-nucleus scattering. *AIP Conf. Proc.*, 1666(1):160001, 2015. doi:10.1063/1.4915590.
- [11] M. Alpizar-Venegas, L. J. Flores, Eduardo Peinado, and E. Vázquez-Jáuregui. Exploring the standard model and beyond from the evidence of CE ν NS with reactor antineutrinos in CONUS+. *Phys. Rev. D*, 111(5):053001, 2025. arXiv:2501.10355, doi:10.1103/PhysRevD.111.053001.
- [12] N. Ackermann et al. New constraints on physics within and beyond the standard model from the latest CONUS datasets, 5 2026. arXiv:2605.22815.
- [13] Xiao-Gang He, Girish C. Joshi, H. Lew, and R. R. Volkas. Simplest Z-prime model. *Phys. Rev. D*, 44:2118–2132, 1991. doi:10.1103/PhysRevD.44.2118.
- [14] Pilar Coloma, M. C. Gonzalez-Garcia, Michele Maltoni, João Paulo Pinheiro, and Salvador Urrea. Constraining new physics with Borexino Phase-II spectral data. *JHEP*, 07:138, 2022. [Erratum: *JHEP* 11, 138 (2022)]. arXiv:2204.03011, doi:10.1007/JHEP07(2022)138.
- [15] Sergei Gninenko and Dmitry Gorbunov. Refining constraints from Borexino measurements on a light Z'-boson coupled to L μ -L τ current. *Phys. Lett. B*, 823:136739, 2021. arXiv:2007.16098, doi:10.1016/j.physletb.2021.136739.
- [16] Mehmet Demirci and M. Fauzi Mustamin. Probing light mediators with recent PandaX-4T low-energy electron recoil data. *Phys. Rev. D*, 111(5):055032, 2025. arXiv:2502.20026, doi:10.1103/PhysRevD.111.055032.
- [17] Mehmet Demirci and M. Fauzi Mustamin. Solar neutrino probes of light new physics: Updated limits from LUX-ZEPLIN experiment. *Phys. Rev. D*, 113(5):055036, 2026. arXiv:2603.19467, doi:10.1103/3cn3-rp6j.
- [18] ShivaSankar K. A., Anirban Majumdar, Dimitrios K. Papoulias, Hemant Prajapati, and Rahul Srivastava. Implications of first LZ and XENONnT results: A comparative study of neutrino properties and light mediators. *Phys. Lett. B*, 839:137742, 2023. arXiv:2208.06415, doi:10.1016/j.physletb.2023.137742.
- [19] M. Cadeddu, N. Cargioli, F. Dordei, C. Giunti, Y. F. Li, E. Picciau, and Y. Y. Zhang. Constraints on light vector mediators through coherent elastic neutrino nucleus scattering data from COHERENT.

- JHEP*, 01:116, 2021. [arXiv:2008.05022](#), [doi:10.1007/JHEP01\(2021\)116](#).
- [20] M. Atzori Corona, M. Cadeddu, N. Cargioli, F. Dordei, C. Giunti, Y. F. Li, E. Picciau, C. A. Ternes, and Y. Y. Zhang. Probing light mediators and $(g - 2)_\mu$ through detection of coherent elastic neutrino nucleus scattering at COHERENT. *JHEP*, 05:109, 2022. [arXiv:2202.11002](#), [doi:10.1007/JHEP05\(2022\)109](#).
- [21] S. Navas et al. Review of particle physics. *Phys. Rev. D*, 110(3):030001, 2024. [doi:10.1103/PhysRevD.110.030001](#).
- [22] Tommy Ohlsson. Status of non-standard neutrino interactions. *Rept. Prog. Phys.*, 76:044201, 2013. [arXiv:1209.2710](#), [doi:10.1088/0034-4885/76/4/044201](#).
- [23] O. G. Miranda and H. Nunokawa. Non standard neutrino interactions: current status and future prospects. *New J. Phys.*, 17(9):095002, 2015. [arXiv:1505.06254](#), [doi:10.1088/1367-2630/17/9/095002](#).
- [24] Y. Farzan and M. Tortola. Neutrino oscillations and Non-Standard Interactions. *Front. in Phys.*, 6:10, 2018. [arXiv:1710.09360](#), [doi:10.3389/fphy.2018.00010](#).
- [25] J. Schechter and J. W. F. Valle. Neutrino Masses in SU(2) x U(1) Theories. *Phys. Rev. D*, 22:2227, 1980. [doi:10.1103/PhysRevD.22.2227](#).
- [26] J. W. F. Valle. Resonant Oscillations of Massless Neutrinos in Matter. *Phys. Lett. B*, 199:432–436, 1987. [doi:10.1016/0370-2693\(87\)90947-6](#).
- [27] C. Giunti. General COHERENT constraints on neutrino nonstandard interactions. *Phys. Rev. D*, 101(3):035039, 2020. [arXiv:1909.00466](#), [doi:10.1103/PhysRevD.101.035039](#).
- [28] D. K. Papoulias and T. S. Kosmas. Standard and Nonstandard Neutrino-Nucleus Reactions Cross Sections and Event Rates to Neutrino Detection Experiments. *Adv. High Energy Phys.*, 2015:763648, 2015. [arXiv:1502.02928](#), [doi:10.1155/2015/763648](#).
- [29] J. Barranco, O. G. Miranda, and T. I. Rashba. Probing new physics with coherent neutrino scattering off nuclei. *JHEP*, 12:021, 2005. [arXiv:hep-ph/0508299](#), [doi:10.1088/1126-6708/2005/12/021](#).
- [30] B. C. Canas, E. A. Garces, O. G. Miranda, A. Parada, and G. Sanchez Garcia. Interplay between nonstandard and nuclear constraints in coherent elastic neutrino-nucleus scattering experiments. *Phys. Rev. D*, 101(3):035012, 2020. [arXiv:1911.09831](#), [doi:10.1103/PhysRevD.101.035012](#).
- [31] Paul Langacker. The Physics of Heavy Z' Gauge Bosons. *Rev. Mod. Phys.*, 81:1199–1228, 2009. [arXiv:0801.1345](#), [doi:10.1103/RevModPhys.81.1199](#).
- [32] Paul Langacker. *The Standard Model and Beyond*. Taylor & Francis, 2017. [doi:10.1201/b22175](#).
- [33] Eduardo Rojas and Jens Erler. Alternative Z' bosons in E_6 . *JHEP*, 10:063, 2015. [arXiv:1505.03208](#), [doi:10.1007/JHEP10\(2015\)063](#).
- [34] D. K. Papoulias and T. S. Kosmas. COHERENT constraints to conventional and exotic neutrino physics. *Phys. Rev. D*, 97(3):033003, 2018. [arXiv:1711.09773](#), [doi:10.1103/PhysRevD.97.033003](#).
- [35] Yu Zhang, Zhuo Yu, Qiang Yang, Mao Song, Gang Li, and Ran Ding. Probing the $L_\mu - L_\tau$ gauge boson at electron colliders. *Phys. Rev. D*, 103(1):015008, 2021. [arXiv:2012.10893](#), [doi:10.1103/PhysRevD.103.015008](#).
- [36] Matthew D. Schwartz. *Quantum Field Theory and the Standard Model*. Cambridge University Press, 3 2014. [doi:10.1017/9781139540940](#).
- [37] David Griffiths. *Introduction to Elementary Particles*. Wiley-VCH, 2nd edition, 2008.
- [38] Manfred Lindner, Thomas Rink, and Manibrata Sen. Light vector bosons and the weak mixing angle in the light of future germanium-based reactor CE ν NS experiments. *JHEP*, 08:171, 2024. [arXiv:2401.13025](#), [doi:10.1007/JHEP08\(2024\)171](#).
- [39] N. Ackermann et al. CONUS+ Experiment. *Eur. Phys. J. C*, 84(12):1265, 2024. [Erratum: *Eur.Phys.J.C* 85, 19 (2025)]. [arXiv:2407.11912](#), [doi:10.1140/epjc/s10052-024-13551-6](#).
- [40] Thomas Rink. *Investigating Neutrino Physics within and beyond the Standard Model using CONUS Experimental Data*. PhD thesis, U. Heidelberg (main), 2022. [doi:10.11588/heidok.00031274](#).
- [41] A. Bonhomme et al. Direct measurement of the ionization quenching factor of nuclear recoils in germanium in the keV energy range. *Eur. Phys. J. C*, 82(9):815, 2022. [arXiv:2202.03754](#), [doi:10.1140/epjc/s10052-022-10768-1](#).
- [42] Marica Baldoncini, Ivan Callegari, Giovanni Fiorentini, Fabio Mantovani, Barbara Ricci, Virginia Strati, and Gerti Xhixha. Reference worldwide model for antineutrinos from reactors. *Phys. Rev. D*, 91(6):065002, 2015. [arXiv:1411.6475](#), [doi:10.1103/PhysRevD.91.065002](#).
- [43] Chao Zhang, Xin Qian, and Muriel Fallot. Reactor antineutrino flux and anomaly. *Prog. Part. Nucl. Phys.*, 136:104106, 2024. [arXiv:2310.13070](#), [doi:10.1016/j.pnpnp.2024.104106](#).

- [44] Th. A. Mueller et al. Improved Predictions of Reactor Antineutrino Spectra. *Phys. Rev. C*, 83:054615, 2011. [arXiv:1101.2663](#), [doi:10.1103/PhysRevC.83.054615](#).
- [45] V. I. Kopeikin. Flux and spectrum of reactor antineutrinos. *Phys. Atom. Nucl.*, 75:143–152, 2012. [doi:10.1134/S1063778812020123](#).
- [46] V. De Romeri, O. G. Miranda, D. K. Papoulias, G. Sanchez Garcia, M. Tórtola, and J. W. F. Valle. Physics implications of a combined analysis of COHERENT CsI and LAr data. *JHEP*, 04:035, 2023. [arXiv:2211.11905](#), [doi:10.1007/JHEP04\(2023\)035](#).
- [47] O. G. Miranda, D. K. Papoulias, G. Sanchez Garcia, O. Sanders, M. Tórtola, and J. W. F. Valle. Implications of the first detection of coherent elastic neutrino-nucleus scattering (CEvNS) with Liquid Argon. *JHEP*, 05:130, 2020. [Erratum: *JHEP* 01, 067 (2021)]. [arXiv:2003.12050](#), [doi:10.1007/JHEP05\(2020\)130](#).